Supplementary Information for

Electromagnetic Simulation Integrated Strategy to Metamorphose Commercial Cotton into Multifunctional Electromagnetic Interference Shielding Fabrics

Athira Rajan[1], Sibi K. S.[1], and Subodh G.[1*]

[1]Department of Physics, University of Kerala, Thiruvananthapuram 695 581, Kerala, India

*Corresponding author: gsubodh@gmail.com

Equation for Shielding Effectiveness and Power Coefficients

The shielding due to reflection (SE_R), shielding due to absorption (SE_A), and total shielding effectiveness (SE_T) of a material can be calculated using the following equations.

$$SE_R(dB) = -10log_{10}(1 - |S_{11}|^2) \quad \text{(Eq. S1)}$$

$$SE_A(dB) = -10log_{10}\left(\frac{|S_{21}|^2}{1-|S_{11}|^2}\right) \quad \text{(Eq. S2)}$$

$$SE_T(dB) = SE_R + SE_A + SE_M \quad \text{(Eq. S3)}$$

where (S_{11}, S_{22}) are the reflection and (S_{21} and S_{12}) are the transmission scattering parameters. The shielding due to multiple internal reflections (SE_M) can be counted as a part of SE_A when the SE_A value exceeds 10 dB [1].

The power coefficients, R, A, T, and $A_{effective,}$ can be calculated from the scattering parameters using the equations.

$$\mathrm{R} = |S_{11}^2| \quad \text{(Eq. S4)}$$

$$\mathrm{T} = |S_{12}^2| \quad \text{(Eq. S5)}$$

$$\mathrm{A} = 1 - \mathrm{R} - \mathrm{T} \quad \text{(Eq. S6)}$$

$$\mathrm{A_{effective}} = \frac{1-\mathrm{R}-\mathrm{T}}{1-\mathrm{R}} \quad \text{(Eq. S7)}$$

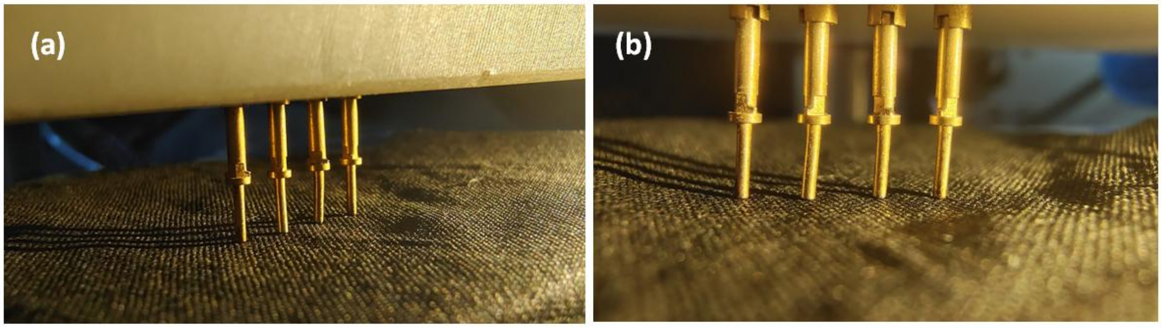

Fig. S1 Four-probe electrical conductivity measurement setup with the PSCC-S0 shielding fabric as the material under test.

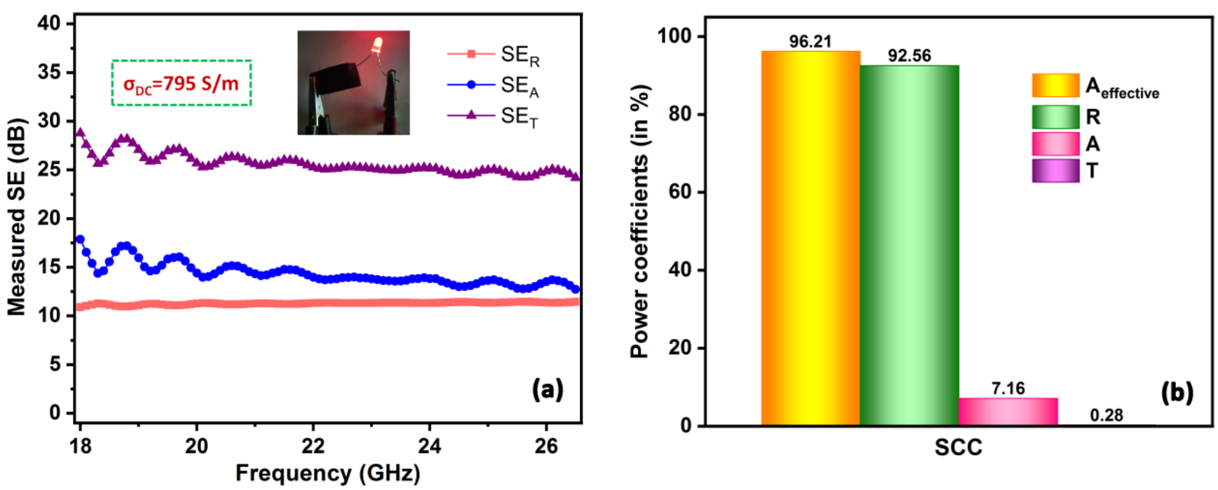

Fig. S2 EMI shielding performance and power coefficients of SCC fabric. **a** Frequency dispersion curves SE_R, SE_A and SE_T of SCC fabric. Inset shows the demonstration of electrical conductivity of SCC fabric. **b** Power coefficients of SCC fabric.

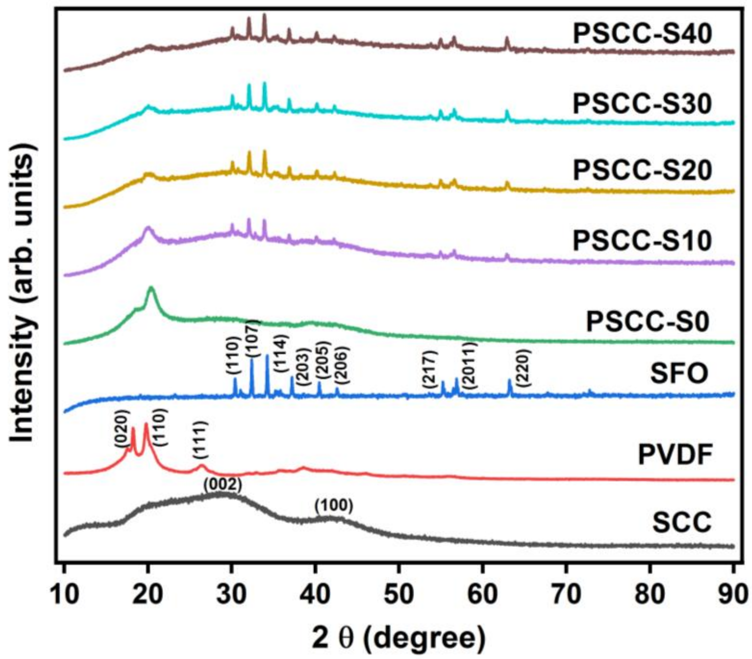

Fig. S3 XRD patterns of SCC, PVDF, SFO and PSCC-Sx (x=0-40) fabrics.

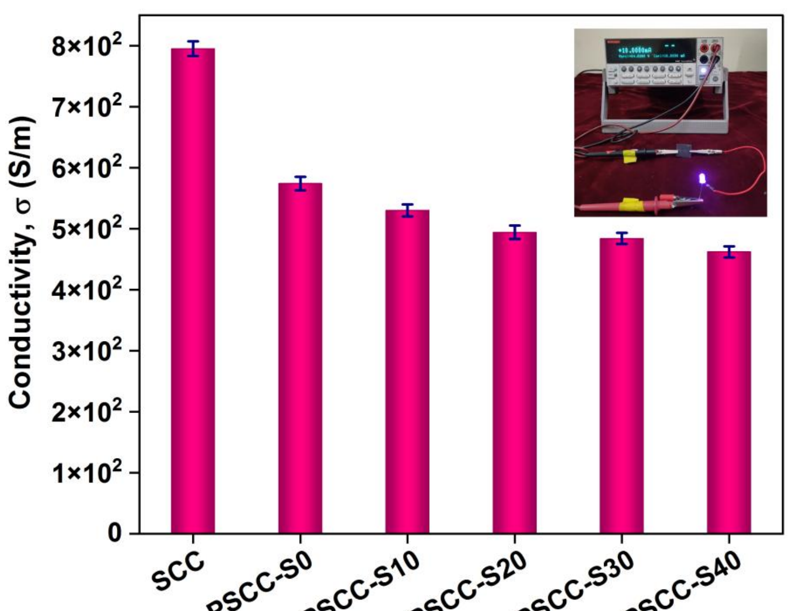

Fig. S4 Electrical conductivity of SCC and PSCC-Sx (x=0-40) fabrics (inset shows the electrical conductivity demonstration of PSCC-S40 fabric).

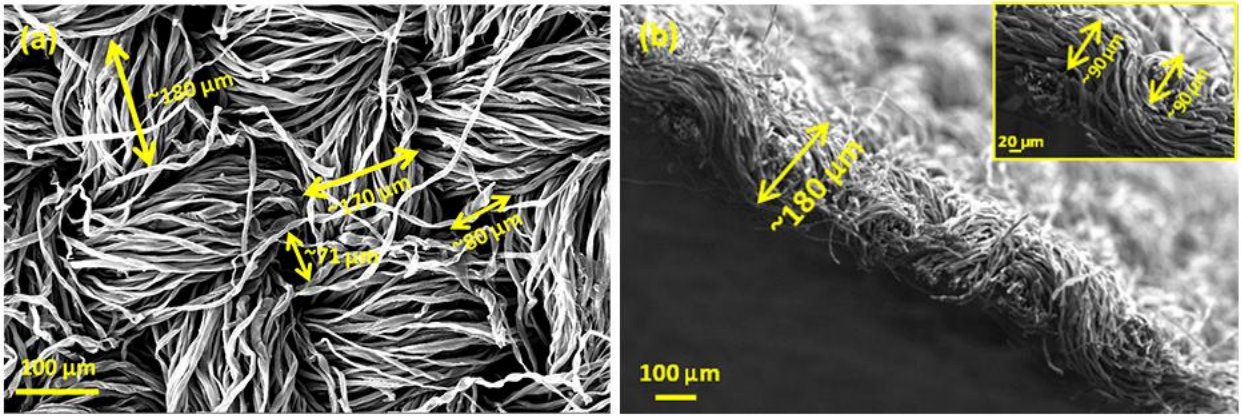

Fig. S5 a Surface morphology of weft-warp weaves in SCC fabric and, **b** SEM image demonstrating thickness of SCC fabric (inset shows the thickness of weft and warp).

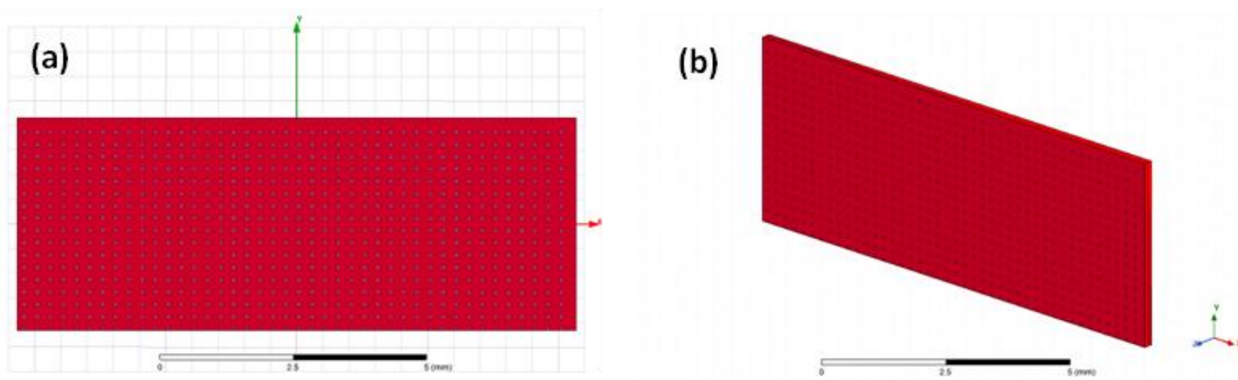

Fig. S6 a Fabric model used for the simulation of PSCC-Sx(x=0-40) fabrics in XY plane and, **b** oblique view of the fabric model.

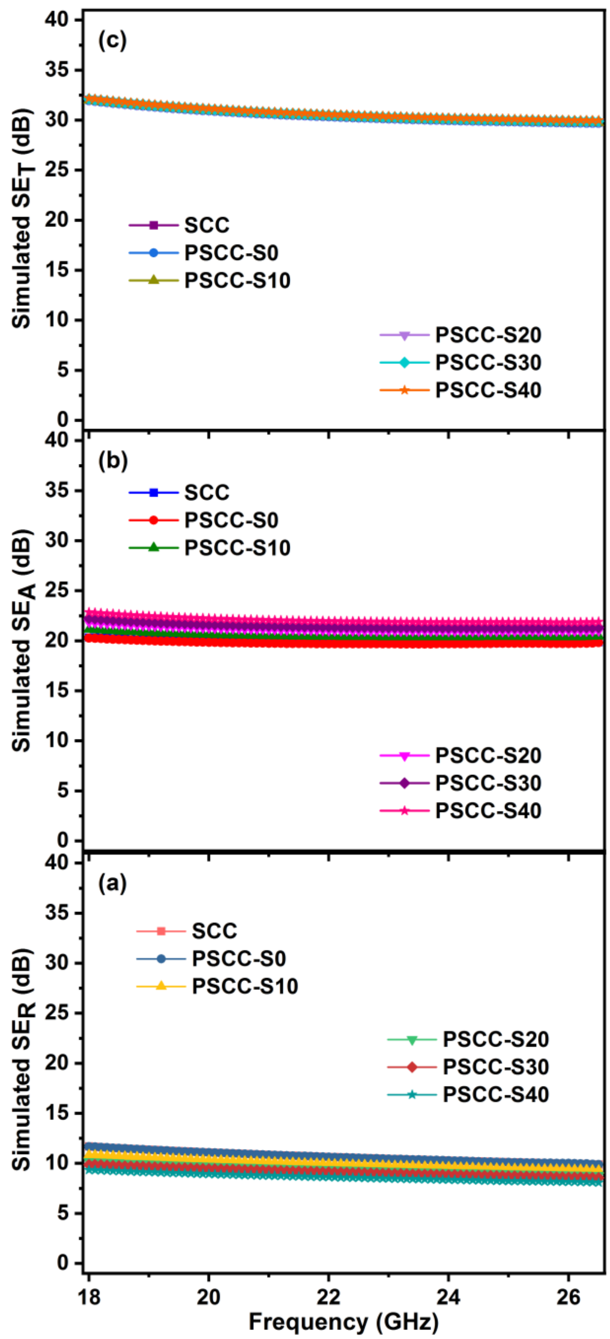

Fig. S7 The frequency response of simulated **a** SE_R, **b** SE_A, and **c** SE_T of SCC and PSCC-Sx (x=0-40) fabrics in the K-band region.

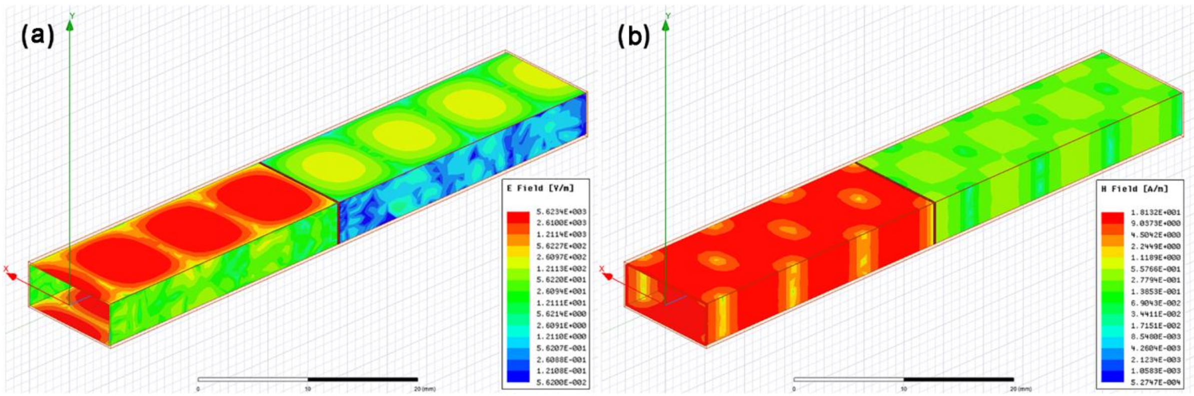

Fig. S8 Electromagnetic field distribution inside virtual waveguide measurement environment. **a** Electric field intensity distribution inside the waveguide with PSCC-S40 fabric as the electromagnetic shielding test subject. **b** Magnetic field intensity distribution inside the waveguide with PSCC-S40 fabric as the electromagnetic shielding test subject.

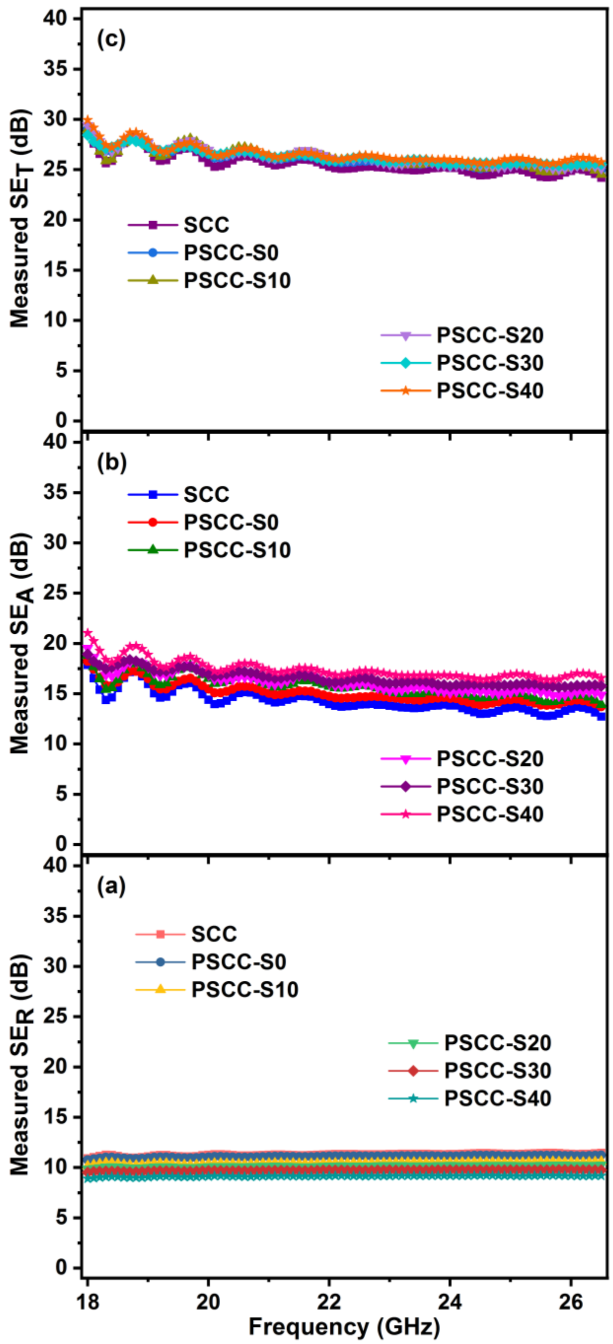

Fig. S9 The frequency response of measured **a** SE_R, **b** SE_A, and **c** SE_T of SCC and PSCC-Sx (x=0-40) fabrics in the K-band region.

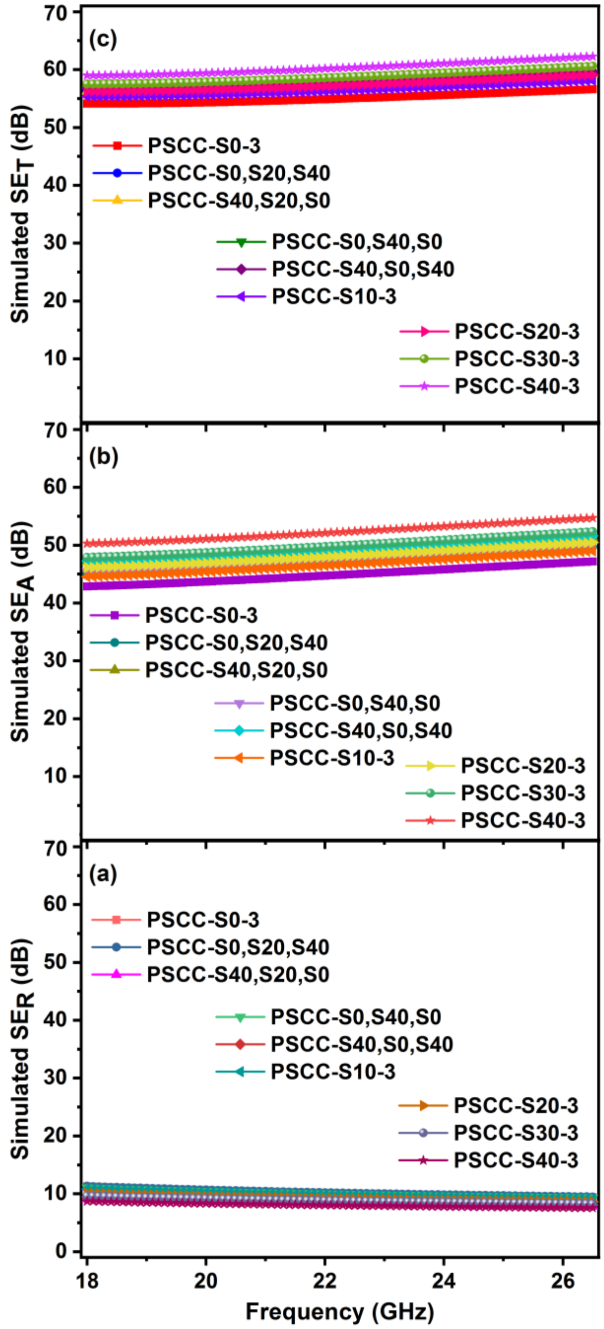

Fig. S10 The simulated frequency response of **a** SE_R, **b** SE_A, and **c** SE_T of various layered configurations of PSCC shielding structures in the K-band region.

Analysis of Shielding Performance of Simulated Homogenous and Heterogeneous Layered Structures

To gain a thorough understanding, let us first analyze the shielding performance of the layered structures in two sections, viz., homogenous layering and heterogeneous layering. Among the homogenous layering, the predicted SE_T of the shielding structures is in the order PSCC-S0-3 < PSCC-S10-3 < PSCC-S20-3 < PSCC-S30-3 < PSCC-S40-3, as per Fig. S10. The SE_A of the structures is in the same order, while the SE_R is in the opposite order. It is interesting to recall that the total shielding effectiveness of all the single layers was approximately the same. However, when the strategy of multiple-layer arrangement was introduced, the difference in shielding performance between PSCC-S0-3 and PSCC-S40-3 was found to be approximately 5 dB, with the increment in SE_A being ~ 7 dB and reduction in SE_R being ~2 dB. If we nullify the multiple internal reflections between the layers, which will be common in all structures, the enhancement in electromagnetic energy absorption can be attributed to the presence of ferrite in each layer of PSCC-S40-3 compared to PSCC-S0-3. The probability of EM waves entering the fabric structure will be higher in the case of PSCC-S40 than PSCC-S0 due to its reduced conductivity and increased permeability.

The thickness of the shield should also be considered when comparing the EMI shielding properties of materials. In the case of PSCC-S40 and PSCC-S0 with respective thicknesses of 0.25 and 0.21 mm, the thickness difference arises from the ferrite-PVDF layer as the base material (SCC) is the same. This layer is a non-conducting coating layer with magnetic properties. Here, the difference in thickness between PSCC-S0-3 and PSCC-S40-3 is 0.12 mm, which entirely corresponds to ferrite-PVDF coating layers. However, the observations from the literature suggest that hexaferrite-PVDF layers with even 0.5 mm thickness and comparable EM properties to that of the SFO-PVDF layer exhibit very poor EMI shielding performance [2]. Thus, we can deduce that the mere thickness enhancement does not contribute to the enhanced shielding of the PSCC-S40-3 structure. It is the amalgamation of the improved impedance matching mechanism provided by the ferrite, along with the conductivity of the base material, which leads to the shielding enhancement. At each interface of the layers, the enhanced impedance matching provided by the ferrite reduces the reflection and allows the EM wave to pass through the layer. Then, the EM wave will undergo attenuation due to various mechanisms, such as the multiple internal reflections at the ferrite-PVDF-SCC layer interfaces, magnetic losses, dielectric losses and conductive losses. This process repeats three times as the wave passes through the three-layered PSCC-S40-3 structure, endowing the structure with enhanced EM wave absorption ability. In the case of the PSCC-S0-3 structure, at the primary interface, the reflections will reduce the probability of admission of EM waves into the material, and the absence of magnetic losses, along with the lower dielectric losses, reduce its wave absorption capability as well. Hence, in the case of the PSCC-S0-3 layer, the amount of primary reflection will always be higher. As we examine the EMI shielding performance of various homogenous PSCC-Sx (x=0-40) structures based on SE_A and SE_R, we can see that there is a progressive enhancement in SE_A and a reduction in SE_R as we move from PSCC-S0-3 to PSCC-S40-3, validating the effect of improved impedance matching in the structures.

In the case of heterogeneous layered structures, the simulated SE_T of PSCC-S0,S20,S40, PSCC-S40,S20,S0, PSCC-S0,S40,S0 and PSCC-S40,S0,S40 is comparable, with the best one being PSCC-S40,S0,S40. The only variation that can be observed in the EMI shielding performance of these structures is the difference between SE_R and SE_A. In the case of SE_R, the heterogeneous layered structures take the order of PSCC-S0,S20,S40 ≈ PSCC-S0,S40,S0 > PSCC-S40,S0,S40 ≈ PSCC-S40,S20,S0 and SE_A takes the reverse order. However, the enhancement in SE_A or the reduction in SE_R between these structures is rather low (<2 dB), which indicates that the shielding properties of structures could not be enhanced to a large extent when the conductivities of the layer are within the same range (same order of magnitude). This observation is very relevant since the literature suggests that heterogeneous multiple-layer arrangement positively enhances the shielding performance of shielding structures, which is not observed in this study. However, it can be noted that the conductivity of the magnetic and conductive layers discussed in those studies were at least two orders of magnitude apart [2-4]. Here, there is no drastic distinction between the conducting-magnetic-conducting (CMC) arrangement (PSCC-S0,S40,S0) and magnetic-conducting-magnetic (MCM) arrangement (PSCC-S40,S0,S40) in terms of conductivity, which leads to similar shielding properties. The presence of the magnetic PSCC-S40 layer is the reason for the mere rise or dip of SE_R and SE_A, respectively. For example, in the case of PSCC-S0,S40,S0 (or PSCC-S0,S20,S40), the first layer is devoid of any magnetic enhancement, which will give rise to an increased SE_R and decreased SE_A as primary reflection of EM radiation will be higher in these structures, whereas in the case of PSCC-S40, S0, S40 (or PSCC-S40, S20, S0) the first layer is the one with the highest permeability among all the other shielding structures, which will lead to higher impedance matching and reduced primary reflections. Now, let's compare the shielding properties of the heterogeneous and homogenous multilayered PSCC structures. From Fig. S10, it is evident that the homogenous structures with higher ferrite content exhibited the highest SE_T. This enhancement is simply due to the higher attenuation of EM radiation at each layer due to the increased permeability-derived impedance matching and additional losses stemming from the magnetic properties of the ferrite.

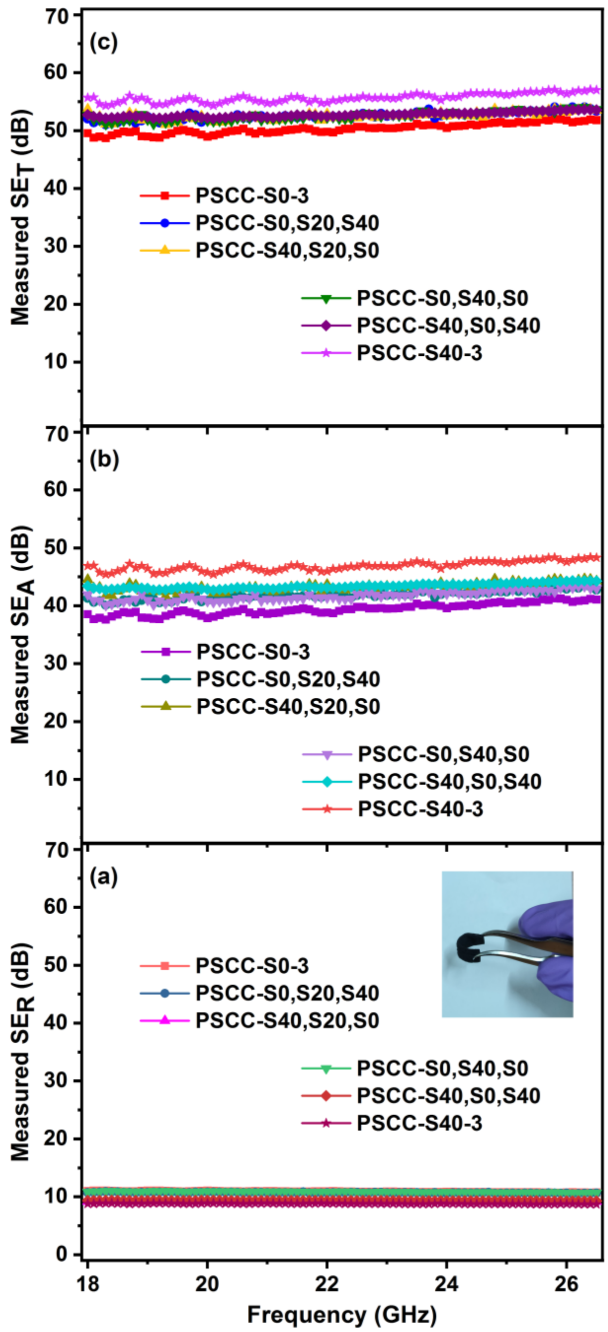

Fig. S11 The measured frequency response of **a** SE_R, **b** SE_A, and **c** SE_T of various layered configurations of PSCC shielding structures in the K-band region. Inset of Fig. S11a demonstrates the flexibility of PSCC-S40-3 fabric.

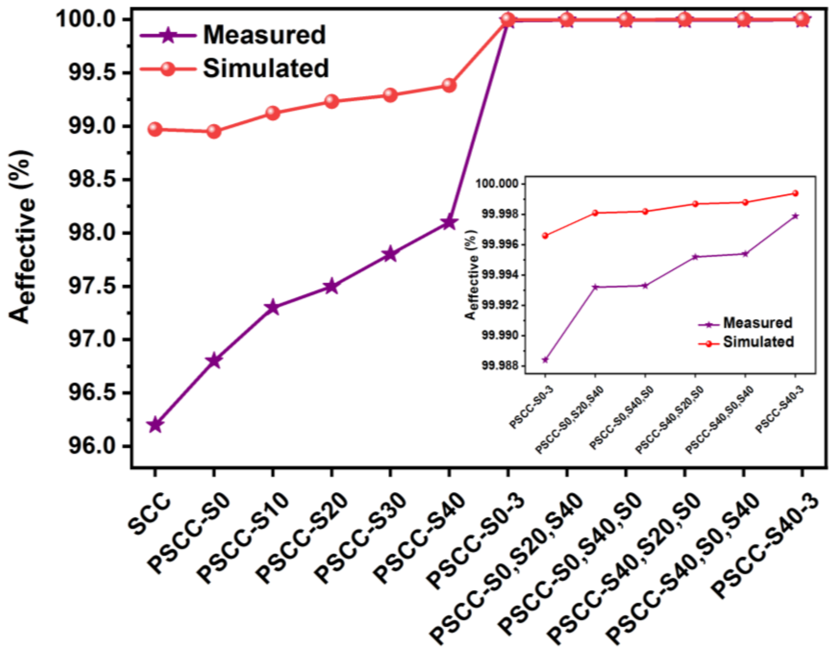

Fig. S12 Representation of $A_{effective}$ of SCC, PSCC-Sx (x=0-40) and layered PSCC fabrics in the K-band region, in percentage.

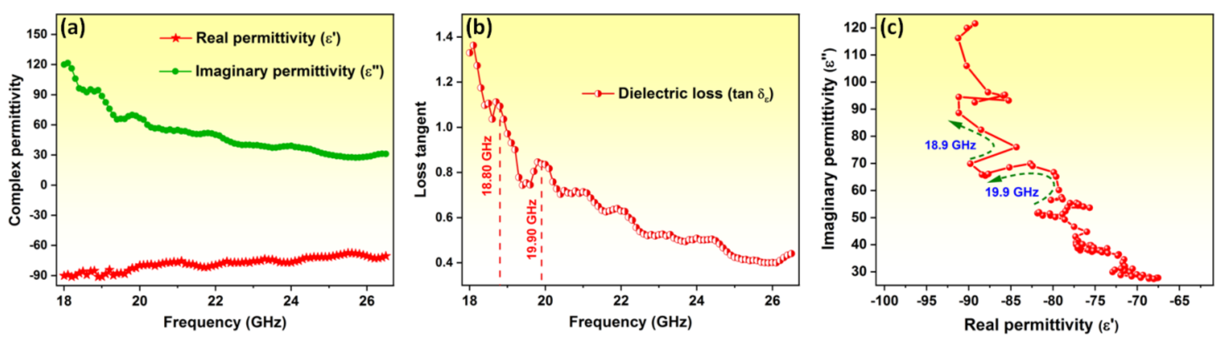

Fig. S13 Dielectric properties and associated parameter analysis of PSCC-S0-3 fabric over the K-band region. **a** Frequency dependence of complex permittivity. **b** Frequency dependence of dielectric loss tangent. **c** Two-dimensional representation of the Cole-Cole plot.

.

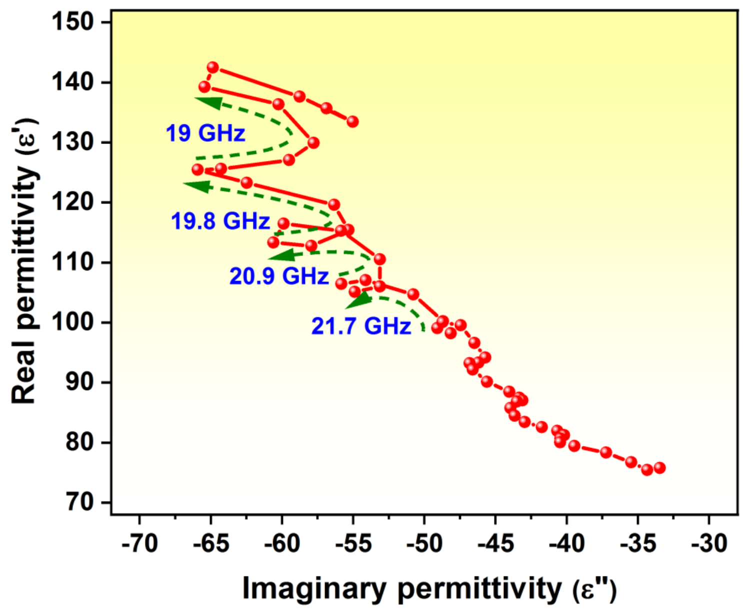

Fig. S14 Cole-Cole plot of PSCC-S40-3 fabric over the K-band region.

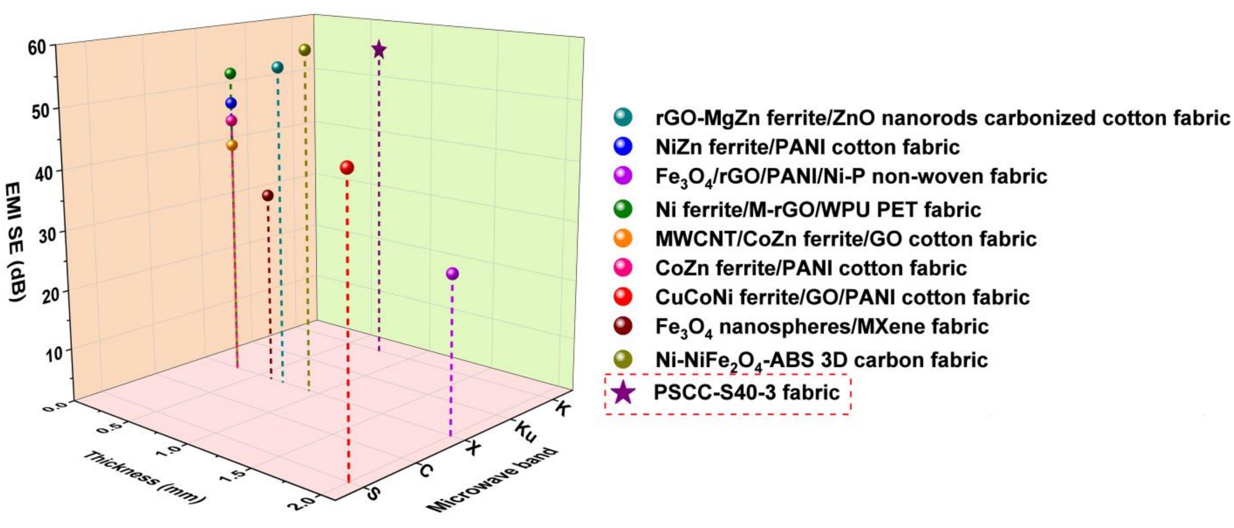

Fig. S15 The comparison of EMI SE of PSSC-S40-3 fabric with recently reported ferrite incorporated shielding fabrics [5-13].

Hydrophobicity of the Shielding Fabrics

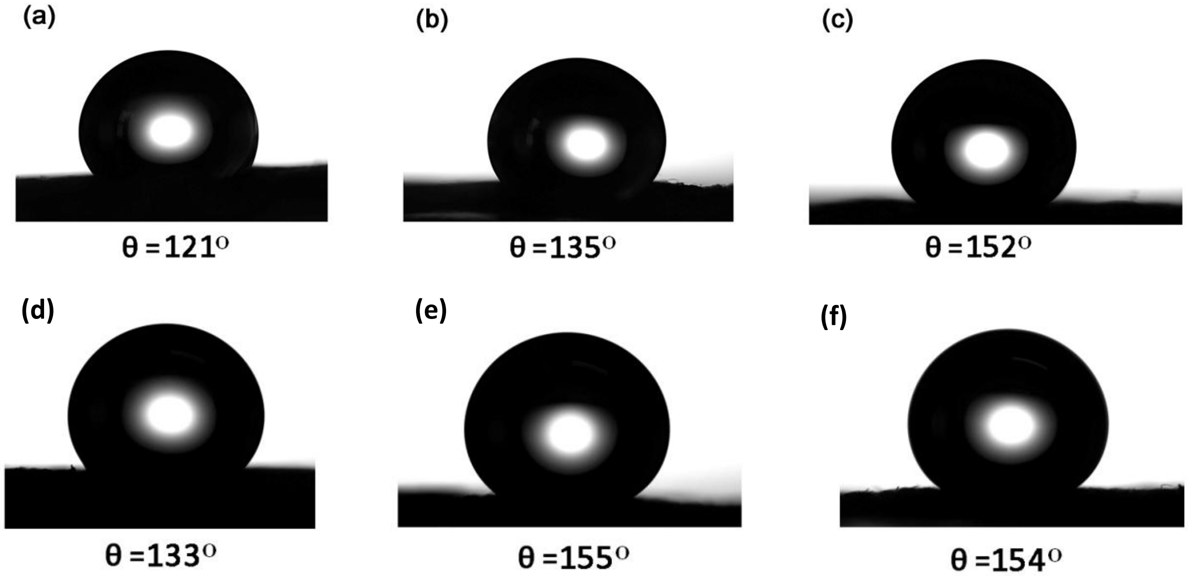

Fig. S16 Hydrophobicity demonstration of shielding fabrics. Contact angle for **a** SCC fabric, **b** PSCC-S0 fabric **c** PSCC-S40 fabric, **d** PSCC-S0-3, **e** PSCC-S40,S0,S40 and **f** PSCC-S40-3

Hydrophobicity is an essential property for a shielding material from a practical application standpoint. In light of this, the surface wettability of selected SCC, PSCC-Sx and layered PSCC fabrics were investigated to understand how polymer and ferrite incorporation modulated wettability. Fig. S16(a-f) exhibits the contact angle (CA) of SCC and PSCC-Sx (x=0 and 40) fabrics and layered fabrics. It can be learnt from the Fig. S16a that the SCC fabric shows a hydrophobic nature with a CA of 121º. However, some spreading of the water droplet can be observed from the image. Compared to scoured cotton, which displayed a hydrophilic nature due to the abundance of functional groups, SCC has very low functional groups, and the small spreading might be due to the residual functional groups present in the fabric even after carbonization. The CA was found to be improved to 135º (Fig. S16b) when PVDF coating was applied to the fabric (PSCC-S0), which is due to the hydrophobic nature of PVDF with low surface energy [14]. It is interesting to note that the hydrophobicity of the fabric appreciably improved on ferrite incorporation, with the CA of PSCC-S40 reaching up to 152º (Fig. S16c), making the fabric superhydrophobic. The superhydrophobicity of the PSCC-S40 fabric can be attributed to the microscale roughness introduced by the ferrite and the low surface energy of the PVDF [15]. Further, PSCC-S0-3, PSCC-S40,S0,S40 and PSCC-S40-3 displayed a CA of 133º, 155º and 154º, respectively, which is in accordance with the CA of the respective top-most layer of the layered PSCC fabrics (Fig. S16d-f). The superhydrophobic nature of the PSSC-S40-3 fabric with exceptional shielding performance makes it highly desirable for outdoor electronic applications and handheld device applications.

Application Demonstration of the Shielding Fabrics

To demonstrate the application potential of the EMI shielding fabrics, two experiments (Demonstration_1 and Demonstration_2) were conducted using the PSCC-S40-3 fabric. In the first experiment (Demonstration_1), an antenna designed to operate at 2.4 GHz frequency (antenna 1-A_1) is placed in an anechoic chamber as the receiver, while a horn antenna covering 800 MHz to 18 GHz (antenna 2-A_2) serves as the transmitter. The two antennas were connected to the two ports of the VNA and the measurement setup was calibrated to minimize errors. In the reference experiment (without the shielding fabric), the S_{11} parameter indicated that the antenna is perfectly radiating near the designed frequency (~2.37 GHz), with S_{11} at the resonant frequency (f_r) around -17 dB. The S_{21} parameter, which measures the power received at A_2 relative to the input power fed to A_1, peaked around the resonant frequency of the antenna (~ -25 dB), confirming proper antenna performance. When the antenna was covered with the PSCC-S40-3 shielding fabric, the S-parameters changed significantly. S_{11} became nearly flat and S_{21} dropped to around -42 dB, indicating that the antenna was no longer radiating at the designed frequency and very little power was being transmitted between the antennas. This change occurred because the highly conductive shielding material interacted with the electromagnetic environment of the antenna and altered its electromagnetic properties, thereby detuning the antenna. This experiment demonstrates how conductive shielding fabrics can modulate antenna performance by altering the electromagnetic characteristics of the antenna.

An additional experiment (Demonstration_2) was conducted using two smartphones (4G) to further demonstrate the practical applicability of the shielding fabric. Initially, a phone call was successfully established between the two phones without any obstructions, confirming normal operation. Then, one of the phones is covered with aluminum foil, leaving an opening at the back of the phone. A second call was then made, and despite having the aluminum foil coverage, the call went through, indicating the phone could still receive the signal through the exposed portion. Next, the PSCC-S40-3 EMI shielding fabric was placed over the opening in the aluminum foil coverage, and a third call was made. This time the call was not connected, indicating that the EMI shielding fabric effectively blocked the microwave radiation and cellular signal reception. This experiment highlights the ability of the EMI shielding fabric to block microwave radiations effectively, showcasing its potential application in shielding mobile phone signals.

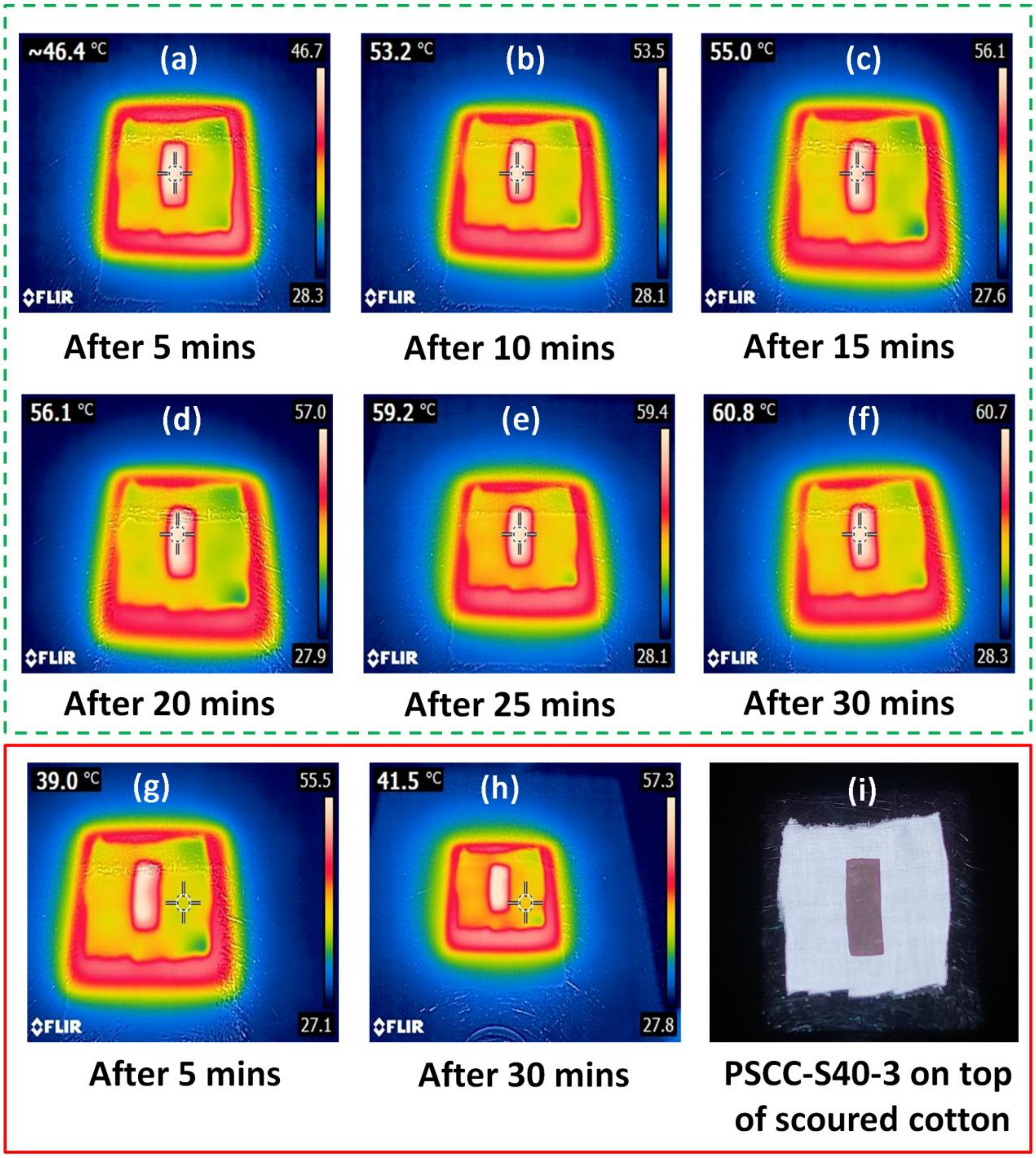

Fig. S17 IR images of PSCC-S40-3 fabric placed above scoured cotton fabric exposed to 1000 W radiation from the solar simulator at **a** 5 mins, **b** 10 mins, **c** 15 mins, **d** 20 mins, **e** 25 mins, and **f** 30 mins and the temperature of scoured cotton after **g** 5 mins and **h** 30 mins and **i** optical image of PSCC-S40-3 fabric placed on top of the cotton fabric under the solar simulator source.

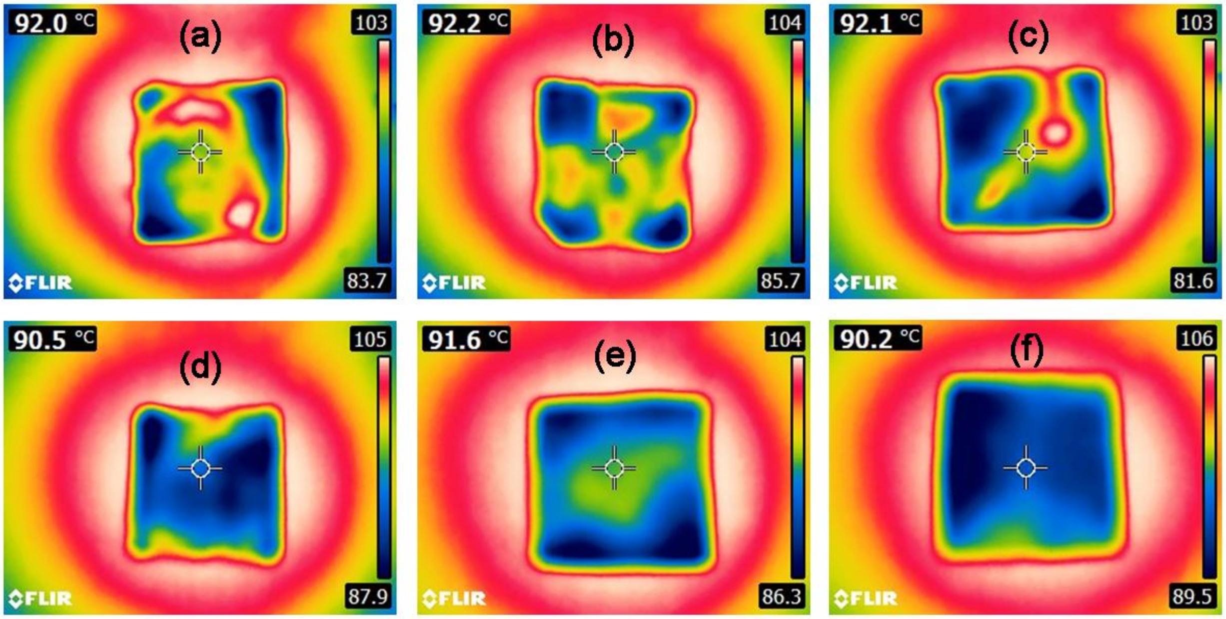

Figure S18. Temperature profiles of **a** SCC, **b** PSCC-S10, **c** PSCC-S40, **d** PSCC-S0-3, **e** PSCC-S40,S0,S40 and **f** PSCC-S40-3 fabrics, respectively, placed on top of a heating plate kept at ~100 ºC.

Table S1. Input parameters used for simulation.

Composition	ε_r	tan δ_ε	μ_r	tan δ_μ	**Conductivity (S/m)**	**Thickness (mm)**
SCC	79.20	0.150	1	0	795	0.180
PS-0	3.02	0.065	1	0	0.011	0.030
PS-10	3.37	0.072	1.15	0.045	0.013	0.040
PS-20	3.42	0.074	1.17	0.068	0.014	0.048
PS-30	3.69	0.082	1.23	0.074	0.016	0.062
PS-40	4.07	0.094	1.34	0.133	0.021	0.070

Table S2. A comparison of multifunctionality and EMI shielding capabilities of various multifunctional flexible EMI shields.

Flexible EMI shield	**Thickness (mm)**	**EMI SE (dB)**	**Frequency band**	**Multifunctionality**	**References**
PVDF film with alternating oriented graphene/Ni nanochains	0.7	51.4	K band	Thermal management ability	[16]
Silicone-coated MXene/ cellulose nanofiber aerogel films	0.54	39.5	X band	Photothermal and Joule heating capability	[17]
Ag NWs/ PDMS-MPI-HDI composites	0.5	32	X band	Self-healing ability and tear resistance	[18]
PEDOT:PSS-Fe_3O_4/PVA hydrogel	1.0	> 46	X band	Strain sensing	[19]
TPU/SiAPP/ SCF/$Ti_3C_2T_x$ MXene composites	1.02	50.5	X band	Fire-resistance	[20]
AgNWs-MXene/PDA polyester fabric	0.6	44	X band	Electrothermal conversion ability and strain/temperature sensing	[21]
CNTs-MXene/PDA-TPU fabric	0.6	43	X band	Strain sensing and Joule heating capability	[22]
Multiwalled carbon nanotube/ PTFE membranes	0.52	42.2	X band	Electrothermal conversion ability	[23]
Carbon fiber felt@nickel composite films	0.4	80	X band	Joule heating capability and thermal management	[24]
High graphene nanoplates-loaded polyurethane (GNP/PU) composites	0.4	67.6	X band	Thermal management ability	[25]
Graphene nanoplatelets incorporated LLDPE laminated Al- Ni foil composite tapes	0.337	45	X band	Tensile strength	[26]
$SrFe_{12}O_{19}$ incorporated multilayered carbonized cotton fabric (PSCC-S40-3)	0.75	55.67	K band	Joule heating capability, thermal management and photothermal performance	This work

References

1. Guo Z, Ren P, Fu B, Ren F, Jin Y, Sun Z (2020) Multi-layered graphene-Fe_3O_4/poly (vinylidene fluoride) hybrid composite films for high-efficient electromagnetic shielding. Polym Test 89:106652. https://doi.org/10.1016/J.POLYMERTESTING.2020.106652
2. Rajan A, K Solaman S, Ganesanpotti S (2023) Design and Fabrication of Layered Electromagnetic Interference Shielding Materials: A Cost-Effective Strategy for Performance Prediction and Efficiency Tuning. ACS Appl Mater Interfaces 15:5822–5835. https://doi.org/10.1021/acsami.2c19016
3. Qi Q, Ma L, Zhao B, Wang S, Liu X, Lei Y, Park CB (2020) An Effective Design Strategy for the Sandwich Structure of PVDF/GNP-Ni-CNT Composites with Remarkable Electromagnetic Interference Shielding Effectiveness. ACS Appl Mater Interfaces 12:36568–36577. https://doi.org/10.1021/acsami.0c10600
4. Amini M, Kamkar M, Rahmani F, Ghaffarkhah A, Ahmadijokani F, Arjmand M (2021) Multilayer Structures of a $Zn_{0.5}Ni_{0.5}Fe_2O_4$-Reduced Graphene Oxide/PVDF Nanocomposite for Tunable and Highly Efficient Microwave Absorbers. ACS Appl Electron Mater 3:5514–5527. https://doi.org/10.1021/acsaelm.1c00940
5. Gupta S, Tripathy AR, Tai N-H (2024) Reduced graphene oxide-manganese ferrite/zinc oxide nanorods coated carbonized cotton fabric for absorption-dominant electromagnetic interference shielding. Surfaces and Interfaces 46:103963. https://doi.org/10.1016/J.SURFIN.2024.103963
6. Kumar S, Kumar P, Gupta R, Verma V (2021) Electromagnetic interference shielding behaviors of in-situ polymerized ferrite-polyaniline nano-composites and ferrite-polyaniline deposited fabrics in X-band frequency range. J Alloys Compd 862:158331. https://doi.org/10.1016/J.JALLCOM.2020.158331
7. Kumar S, Verma V, Walia R (2021) Magnetization and thickness dependent microwave attenuation behaviour of Ferrite-PANI composites and embedded composite-fabrics prepared by in situ polymerization. AIP Adv 11: 015106. https://doi.org/10.1063/9.0000022
8. Kumar S, Walia R, Kumar A, Verma V (2021) Hybrid structure of MWCNT/ferrite and GO incorporated composites for microwave shielding properties and their practical applications.11:9775-9787. https://doi.org/10.1039/D1RA01129D
9. Magisetty RP, Shukla A, Kandasubramanian B (2019) Terpolymer (ABS) cermet (Ni-$NiFe_2O_4$) hybrid nanocomposite engineered 3D-carbon fabric mat as a X-band electromagnetic interference shielding material. Mater Lett 238:214–217. https://doi.org/10.1016/J.MATLET.2018.12.023
10. Sedighi A, Naderi M, Brycki B (2023) Wearable nonwoven fabric decorated with Fe_3O_4/rGO/PANI/Ni-P for efficient electromagnetic interference shielding. J Alloys Compd 938:168454. https://doi.org/10.1016/J.JALLCOM.2022.168454
11. Sun J, Wang L, Yang Q, Shen Y, Zhang X (2020) Preparation of copper-cobalt-nickel ferrite/graphene oxide/polyaniline composite and its applications in microwave absorption coating. Prog Org Coatings 141:105552. https://doi.org/10.1016/J.PORGCOAT.2020.105552
12. Wang Y, Song Y, Qi Q, Wang W, Yu D (2019) Robustly magnetic and conductive textile with high electromagnetic shielding performance prepared by synchronous thiol-ene click chemistry. Ind Eng Chem Res

58:23154–23165. https://doi.org/10.1021/acs.iecr.9b05461

13. Zheng X, Tang J, Cheng L, Yang H, Zou L, Li C (2023) Superhydrophobic hollow magnetized Fe_3O_4 nanospheres/MXene fabrics for electromagnetic interference shielding. J Alloys Compd 934:167964. https://doi.org/10.1016/J.JALLCOM.2022.167964
14. Wang FJ, Li CQ, Tan ZS, Li W, Ou JF, Xue MS (2013) PVDF surfaces with stable superhydrophobicity. Surf Coatings Technol 222:55–61. https://doi.org/10.1016/J.SURFCOAT.2013.02.004
15. Jonas AM, Cai R, Vermeyen R, Nysten B, Vanneste M, De Smet D, Glinel K (2020) How roughness controls the water repellency of woven fabrics. Mater Des 187:108389. https://doi.org/10.1016/J.MATDES.2019.108389
16. Liang L, Xu P, Wang Y, Shang Y, Ma J, Su F, Feng Y, He C, Wang Y, Liu C (2020) Flexible polyvinylidene fluoride film with alternating oriented graphene/Ni nanochains for electromagnetic interference shielding and thermal management. Chem Eng J 395:125209. https://doi.org/10.1016/J.CEJ.2020.125209
17. Xin W, Ma MG, Chen F (2021) Silicone-Coated MXene/Cellulose Nanofiber Aerogel Films with Photothermal and Joule Heating Performances for Electromagnetic Interference Shielding. ACS Appl Nano Mater 4:7234–7243. https://doi.org/10.1021/ACSANM.1C01185
18. Sun F, Xu J, Liu T, Li F, Poo Y, Zhang Y, Xiong R, Huang C, Fu J (2021) An autonomously ultrafast self-healing, highly colourless, tear-resistant and compliant elastomer tailored for transparent electromagnetic interference shielding films integrated in flexible and optical electronics. Mater Horizons 8:3356–3367. https://doi.org/10.1039/D1MH01199E
19. Hao M, Wang Y, Li L, Lu Q, Sun F, Li L, Yang X, Li Y, Liu M, Feng S, Feng S, Zhang T (2021) Stretchable multifunctional hydrogels for sensing electronics with effective EMI shielding properties. Soft Matter 17:9057–9065. https://doi.org/10.1039/D1SM01027A
20. Chen K, Feng Y, Shi Y, Wang H, Fu L, Liu M, Lv Y, Yang F, Yu B, Liu M, Song P (2022) Flexible and fire safe sandwich structured composites with superior electromagnetic interference shielding properties. Compos Part A Appl Sci Manuf 160:107070. https://doi.org/10.1016/J.COMPOSITESA.2022.107070
21. Zhao W, Zheng Y, Qian J, Zhaofa Z, Jin Z, Qiu H, Zhu C, Hong X (2022) AgNWs/MXene derived multifunctional knitted fabric capable of high electrothermal conversion efficiency, large strain and temperature sensing, and EMI shielding. J Alloys Compd 923:166471. https://doi.org/10.1016/J.JALLCOM.2022.166471
22. Zhang D, Yin R, Zheng Y, Li Q, Liu H, Liu C, Shen C (2022) Multifunctional MXene/CNTs based flexible electronic textile with excellent strain sensing, electromagnetic interference shielding and Joule heating performances. Chem Eng J 438:135587. https://doi.org/10.1016/J.CEJ.2022.135587
23. Shao R, Wang G, Chai J, Wang G, Zhao G (2024) Flexible, reliable, and lightweight multiwalled carbon nanotube/polytetrafluoroethylene membranes with dual-nanofibrous structure for outstanding EMI shielding and multifunctional applications. Small 20:2308992. https://doi.org/10.1002/SMLL.202308992
24. Liu S, Yang J, Yu Y, Liang D, Li Y, Si X, Song S, Meng M, Zhang J, Zhang Y (2024) Multifunctional flexible carbon fiber felt@nickel composite films with core–shell heterostructure: Exceptional Joule heating capability, thermal management, and electromagnetic interference shielding. Chem Eng J 494:153221. https://doi.org/10.1016/J.CEJ.2024.153221

25. Li YK, Li WJ, Wang ZX, Du PY, Xu L, Jia LC, Yan DX (2023) High-efficiency electromagnetic interference shielding and thermal management of high-graphene nanoplate-loaded composites enabled by polymer-infiltrated technique. Carbon 211:118096. https://doi.org/10.1016/J.CARBON.2023.118096
26. Chandra RBJ, Shivamurthy B, Gowda SBB, Kumar MS (2023) Flexible Linear Low-density Polyethylene Laminated Aluminum and Nickel Foil Composite Tapes for Electromagnetic Interference Shielding. Eng Sci 21:. https://doi.org/10.30919/ES8D777